

Article

In Situ Study on Dehydration and Phase Transformation of Antigorite

Shuang Liang^{1,2}, Yuegao Liu¹  and Shenghua Mei^{1,*}

¹ CAS Key Laboratory for Experimental Study under Deep-Sea Extreme Conditions, Institute of Deep-Sea Science and Engineering, Chinese Academy of Sciences, Sanya 572000, China; liangs@idsse.ac.cn (S.L.); liuyg@idsse.ac.cn (Y.L.)

² University of Chinese Academy of Sciences, Beijing 100049, China

* Correspondence: mei@idsse.ac.cn

Abstract: Antigorite is the main carrier of water in Earth's subduction zones. The dehydration processes of antigorite were investigated by carrying out in situ phase transition experiments using a dynamic diamond anvil cell, with a time-resolved Raman scattering system, at 0.3–10 GPa and 396–1100 K. Three typical phase transformation reactions occurred within the P – T range of this study, corresponding to three reaction products. At low pressures (<0.7 GPa), antigorite transfers to talc and forsterite; as the temperature increases, the talc disappears and a combination of forsterite and clinoenstatite occurs. At moderate pressures (1.8–7.5 GPa), antigorite dehydrates into forsterite and clinoenstatite as temperatures increase; with the continuous increase in pressure, the dehydration products become clinoenstatite and phase A. At high pressures (>8.6 GPa), the products of the dehydration phase transition of antigorite are consistently clinoenstatite and phase A. Compared with the previous studies carried out by large-volume presses (such as a multi anvil press and a piston-cylinder press), the reaction to produce phase A occurs at higher P – T conditions, and the stable temperature region for talc as a dehydration product is narrower. Moreover, large quantities of pores with 5–10 μm in diameter formed in dehydration products, supporting the hypothesis that intermediate-depth earthquakes may result from dehydration embrittlement. The precise phase boundary determined by this in situ study provides a better understanding of the dehydration phase transition behavior and geological phenomena exhibited by antigorite under different pressure and temperature conditions.

Keywords: antigorite; dehydration phase transition; dynamic diamond anvil cell (dDAC); dehydration embrittlement; in situ raman experiment



Citation: Liang, S.; Liu, Y.; Mei, S. In Situ Study on Dehydration and Phase Transformation of Antigorite. *Minerals* **2022**, *12*, 567. <https://doi.org/10.3390/min12050567>

Academic Editor: Shoji Arai

Received: 1 March 2022

Accepted: 13 April 2022

Published: 30 April 2022

Publisher's Note: MDPI stays neutral with regard to jurisdictional claims in published maps and institutional affiliations.



Copyright: © 2022 by the authors. Licensee MDPI, Basel, Switzerland. This article is an open access article distributed under the terms and conditions of the Creative Commons Attribution (CC BY) license (<https://creativecommons.org/licenses/by/4.0/>).

1. Introduction

Serpentine from hydrothermal alteration of ultramafic rocks is the main water-bearing phase (containing 13 wt.% water) in oceanic plates, upper mantle, and mantle wedge associated closely with subduction zones [1]. Oceanic plate subduction can transport large amounts of serpentine to mantle. Serpentine dehydration plays an important role in the water cycle and transport of elements in the subduction zone, the formation of deep-intermediate earthquakes, and the generation of island arc magmas [2–6]. Due to variations in chemical composition and differences in curvature between octahedral and tetrahedral layers, serpentine can be subdivided into chrysotile, lizardite, antigorite, and polygonal serpentine. Antigorite is the most common type of serpentine in the subduction zones [7]. The highest pressure of the stability domain of antigorite is much higher than the other kinds of serpentine [8]. The structure of antigorite is a 1:1 lamellar structure, and each layer consists of some tetrahedral units and octahedral units in a lamellar stack with a periodic wavy lamellar appearance (Figure 1) [2,9].

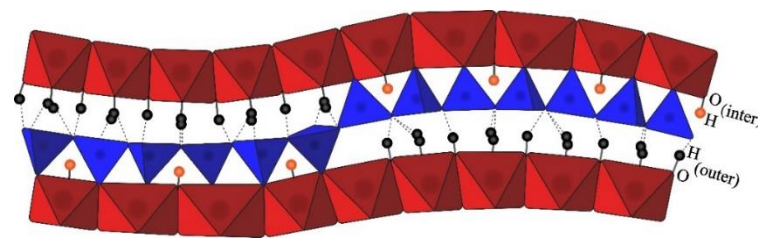


Figure 1. Crystal structure of antigorite. This figure is modified from Bailey (1988) [10]. The blue and red polyhedrons represent silicon-oxygen tetrahedra and magnesium-oxygen octahedral, respectively. The hydrogen atoms of the external hydroxyl and internal hydroxyl are shown in black and orange, respectively. The dashed lines indicate the weak interaction forces between the layered silicates.

It is well known that a small amount of water can strongly affect the conductivity, seismic wave velocity, and rheological strength of the mantle, as well as the migration and distribution of elements in the Earth’s interior [3,11–17]. In actuality, quite a few geological activities (such as volcanoes, earthquakes, etc.) which originate or are initiated in the subduction zone are directly related to the dehydration of water-bearing minerals, including antigorite. Thus, it is of great scientific significance to better understand the dehydration process of antigorite.

Due to its importance, the dehydration phase transition of antigorite has been intensely studied in the past few decades; some results from experimental studies are summarized in Figure 2. To date, it is generally accepted that, in terms of pressure, there are three dehydration processes of antigorite [17]:

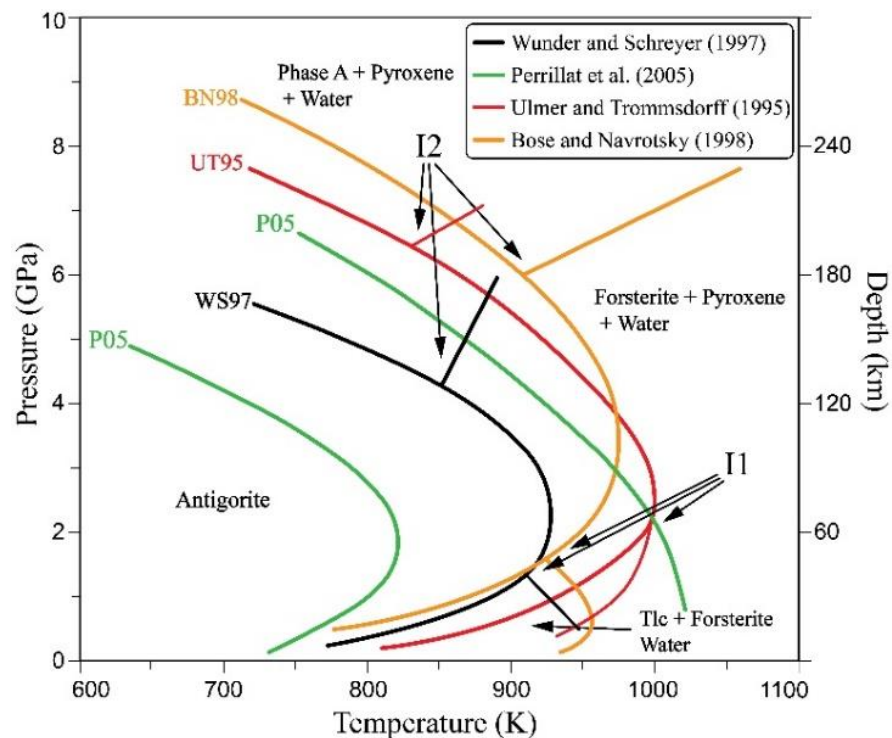


Figure 2. A summary of previous results on the dehydration process of antigorite. WS97: Wunder and Schreyer (1997) [18]; P05: Perrillat et al. (2005) [19]; UT95: Ulmer and Trommsdorff (1995) [17]; and BN98: Bose and Navrotsky (1998) [20].

At low pressures,



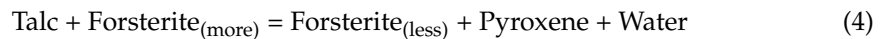
at moderate pressures,



at high pressures,



Moreover, to determine the precise phase boundary related to antigorite dehydration, a two phase boundary reaction without antigorite is necessary (Figure 2):



Though great progress has been made in this field, current understanding on the process of antigorite based on previous studies is still far from satisfactory. As shown in Figure 2, there are at least two deficiencies that need to be improved through further research.

First, the boundaries among the five equation in the dehydration process of antigorite have not been well determined. If we denote the point at which antigorite coexists with the products of reactions 1 and 2 (the intersection of the trend line of reactions 1 and 2) as point I1, and the point at which antigorite coexists with the products of equation 2 and 3 (the intersection of the trend line of Equations (2) and (3) as point I2 (Figure 2), the locations of I1 and I2 for antigorite, in the P - T phase diagram, identified by previous studies remain under dispute. As indicated in Figure 2, the results by a multi anvil press from Bose and Navrotsky (1998) [20] concluded that I1 and I2 are at 1.8 GPa/928 K and 5.8 GPa/893 K, respectively [20]; the results by a piston-cylinder press from Ulmer and Trommsdorff (1995) showed that I1 and I2 are at 2.1 GPa/988 K and 6.6 GPa/843 K, respectively [17]; the results by a piston-cylinder press from Wunder and Schreyer (1997) [18] showed I1 and I2 are at 1.4 GPa/913 K and 4.3 GPa/853 K, respectively. Although the points determined by different studies are different, the results of Perrillat (2005) from experiments carried out with multi anvil press show that these reactions have no intersection, that is, points I1 and I2 do not even exist.

Secondly, there are great differences in previous studies. For example, at 720 K, Equation (3) occurs at around 9 GPa by the result of Bose and Navrotsky (1998) [20] (BN98) and 5.2 GPa by the results of Wunder and Schreyer (1997) [18] (WS97). The results of the two studies differed by 3.8 GPa, which corresponds to ~125 km depth in the Earth. Such a large discrepancy limits our understanding of deep Earth. Although this difference may be due to the different compositions of the samples used in their studies, the composition itself should not be the main reason for this difference. It has been found that the pressure for the dehydration phase transition of antigorite increases with the increase in aluminum content and decreases with the increase in iron content [18,21]. We still take the above two studies as examples. The contents of aluminum and iron (aluminum, wt.%; iron, wt.%) in the samples used in BN98 and WS97 were (0.54, 3.28) and (0.68, 1.66), respectively. While the aluminum content in the two studies was very similar, the iron content in the WS97 sample was much lower than that in the BN98 sample. If the iron content has a significant influence, the pressure for the dehydration phase transition in BN98 should be lower than that in WS97, but the results show the opposite. Thus, even the effect of composition should not be neglected, there must be other reasons for the pronounced differences in previous studies, which is worthy of in-depth exploration.

The differences in experimental methods, especially the lack of in situ observations, in previous experiments may be the main reason for the large inconsistency in the phase boundaries for antigorite. The piston-cylinder press and the multi anvil press both have noticeable errors in temperature and/or pressure. Moreover, observations after the samples have been quenched might lead to inaccurate results of the experimental analysis due to the possibility of phase change reactions reversing during quenching.

To provide a better understanding on the thermo-pressure stability behavior of antigorite, we carried out an in situ study with heated diamond anvil cell (DAC) plus a dynamic loading pressure apparatus to investigate the dehydration process of antigorite under high P - T conditions. In contrast to conventional quenching experiments, this set-up not only allows observation of mineral disappearance and production during phase transformation with the aid of Raman or infrared spectroscopy, but also allows real-time monitoring of changes in OH peaks at high wavenumber region during antigorite dehydration. In this study, experiments were carried out at 0.3–10 GPa and 396–1100 K. The phase boundaries of the three reactions were determined in situ. Our experimental studies provide new constraints on the controversial phase transition boundaries for the dehydration of antigorite.

2. Experimental Process

2.1. Sample Preparation and Loading

2.1.1. Sample Preparation

Antigorite, $Mg_6[Si_4O_{10}](OH)_8$, is a representative mineral in the serpentine group. In nature, its metal site (Mg) is often substituted with Al and Fe plus some other trace elements. The sample used in this study is a natural Mexican antigorite; its composition of major elements determined by electron microprobe analysis is given in Table 1. Based on analyses from Raman spectroscopy, no chrysotile or lizardite was observed.

Table 1. Composition of antigorite as starting sample (wt.%).

SiO ₂	MgO	Al ₂ O ₃	FeO _T	Cr ₂ O ₃	TiO ₂	MnO	CaO	K ₂ O	Na ₂ O	Total
43.25	37.96	2.96	1.99	0.30	0.67	0.02	0.26	0.01	0.06	87.46

To prepare samples for experiments with diamond anvil cell (DAC), a piece was cut from a sample block and then polished with diamond lapping to a thickness of approximately 50 μ m. The prepared samples, after being cleaned and air-dried, were ready for experiments.

2.1.2. Sample Loading

The high P - T experiments were performed at the CAS Key Laboratory for Experimental Study under Deep-sea Extreme Conditions, Institute of Deep-sea Science and Engineering, Chinese Academy of Sciences (Sanya, Hainan, China). High pressure is produced by the hydrothermal diamond anvil cells (DAC), equipped with two type-IIA low-fluorescence diamonds with culets of 600 μ m to 1000 μ m in diameter (Figure 3). The gaskets were made from rhenium sheets with a thickness of 250 μ m, which were pre-pressed to 100 μ m in thickness. A hole with a diameter of 200 μ m to 340 μ m in the center of rhenium gasket, which was drilled by a Drilex-2000 Laser Hole Puncher (Beijing, China), serves as sample chamber. At room temperature, the sample and pressure calibration material were inserted into the sample chamber by a tungsten probe. Liquid argon, filled with a gas loading device, was used as pressure medium to achieve hydrostatic conditions. After completing the previous work, the DAC was then pressurized to an initial pressure of approximately 0.5 GPa (Figure 3).

2.2. Pressurization and Heating Processes

2.2.1. Heating and Temperature Measurement

Experimental temperature is provided by resistance heating outside the sample. The heating wire was made of 0.1 mm nickel-chromium (Cr₂₀Ni₈₀) resistance wire. The seat is made of silicon nitride, which is more stable than tungsten carbide. During heating, argon gas (a flow rate of 3 L/min) and hydrogen gas (a flow rate of 60 mL/min) were used as protective gases to prevent oxidation of the diamond anvil in the DAC. For a run, target temperature, heating rate (generally ~30 K/min), and duration time can be preset by the controlling system. The temperature near the sample on one side of the diamond anvil

was measured by a K-type thermocouple; the error of measurement was estimated to be ± 0.5 K.

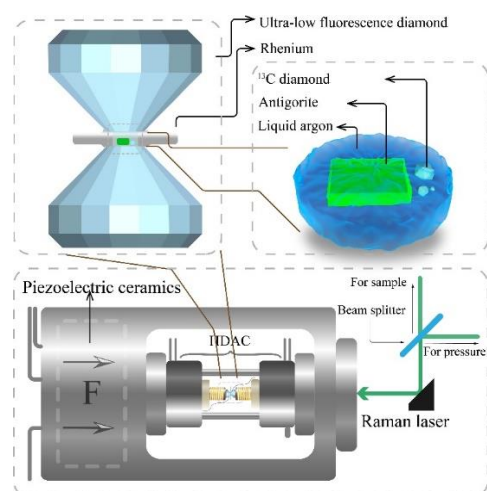


Figure 3. Schematic diagram of experimental details (not to scale). The diamond anvil consists of two ultra-low fluorescence diamonds. Sample and pressure calibration material (^{13}C diamond) are assembled within sample chamber and liquid argon serves as the pressure medium. Pressurization is dynamically controlled by signal-driven piezoelectric ceramics. Raman spectrum is split into two beams by a beam splitter; one is for sample study and one for pressure calibration. In this way, the P – T values and the Raman spectra of samples can be recorded simultaneously.

2.2.2. Pressurization and Pressure Measurement

The target pressure during the experiment was achieved using a dynamic pressure loading device. This was obtained by volume-controllable piezoelectric ceramics (Figure 3). By a connected signal generator, signals of different frequencies were modulated to control the timing of the pressure output, and amplitude is modulated to control the output pressure value. Then, the control signal was transmitted to the piezoelectric ceramic controller to control the expansion behavior of the piezoelectric ceramic. The pressure is determined by the Raman shift of the ^{13}C diamond, which is located next to the sample. The calculation formula [22] is listed as follows:

$$P = 373.97 - 16.55 \times \left[510.41 + \nu_{\text{RC}} - \nu(P, T) + 6.9 \times 10^{-3} \times T - 2.32 \times 10^{-5} \times T^2 \right]^{0.5},$$

where P is the pressure in GPa, T is the temperature in kelvins, ν is the Raman frequency under the real-time pressure and temperature, and ν_{RC} is the Raman frequency at room conditions. The accuracy of pressure measurement with this technique is ± 0.3 GPa [22,23]. The pressure calibration material ^{13}C diamond was synthesized from ^{13}C powder (Cambridge Isotope Laboratories, Inc., Tewksbury, MA, USA, with a purity of 99.99%) at a temperature and pressure of 1800 K and 12 GPa, respectively, by a multi anvil press apparatus at the Southern University of Science and Technology (Figure 4).

To carry out high temperature and high pressure experiments with DAC through external heating is very challenging, especially in pressure control. The main problem is that, during the heating process, the metal gasket of the pressure chamber and the gas as the pressure medium expand during heating, so as to change the preset pressure. Due to the different expansion behaviors of the gasket and gas, the pressure change related to temperature rise is nonlinear and has great uncertainty, so it is difficult to control the pressure at will. In this case, the dynamic loading device provides great convenience. Through the input signal control, the system pressure can be increased or reduced according to the needs, and the target temperature and pressure can be gradually realized through continuous adjustment.

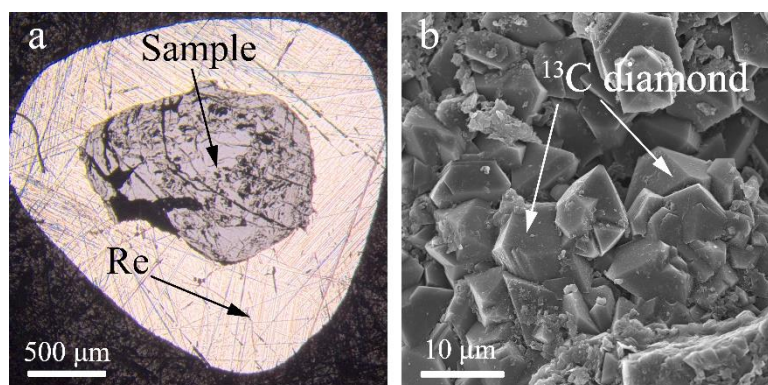


Figure 4. Synthetic ^{13}C diamond from ^{13}C powder at high temperature and pressure. (a) Cross-sectional view of the metal capsule where ^{13}C diamond was synthesized. (b) SEM micrograph of a synthetic ^{13}C diamond sample.

2.3. In Situ Raman Spectroscopy Analyses

2.3.1. Raman Spectroscopy System

Raman spectra were recorded by Raman spectrometer, a confocal microscope Raman spectrometer system with two laser wavelengths, 532 nm and 785 nm. The Raman laser light could be injected into the DAC by a reflector with an angle of 90° (Figure 3). The Raman spectra were recorded by a CCD detector (2000×256 pixels per inch) equipped with an 1800 g mm^{-1} holographic grating and liquid nitrogen cooling system, with a resolution of 1 cm^{-1} . A $20\times$ objective was used to focus the Raman laser with a beam spot diameter of $10 \mu\text{m}$ on a sample. The spectra were acquired with an exposure time between 5 s to 20 s, and the laser output power was between 30 mW and 75 mW depending on signal intensity. The spectrometer was calibrated using a 520.6 cm^{-1} Raman peak in silicon prior to each experimental measurement.

The pressurization time varies from 1000 s to 2000 s. Different gratings were used to maximize the interference of thermal effects. The in situ Raman spectra during the experiments were divided into the low wavenumber region from 100 to 1200 cm^{-1} (silicon oxide tetrahedral stretching signal) and the high wavenumber region from 3200 to 3900 cm^{-1} (OH stretching signal). Separate acquisitions were conducted at low and high wavenumber spectral ranges.

2.3.2. The Basic Raman Spectral Features of Antigorite

The strong Raman peak position near 230 cm^{-1} of antigorite is associated with O-H-O vibrations, where O is the non-bridging oxygen of the SiO_4 tetrahedra and H is the hydrogen of the OH group outside the adjacent layer [24]. The Raman peak at 350 cm^{-1} represents the vibrations of the SiO_4 tetrahedra [25]. The bending vibrational mode of silicon-oxygen tetrahedra in antigorite was reflected at the peak between 377 and 382 cm^{-1} [26]. The weak peak at 620 cm^{-1} in antigorite is reported to be the OH-Mg-OH translation mode [26]. The strong peak near 690 cm^{-1} is another significant strong band attributed to the symmetric stretching mode of the Si-O-Si (bridging oxygen) group [25]. The weak Raman peak at 1045 cm^{-1} is caused by an antisymmetric stretching mode of the Si-Ob-Si group (oxygen bridge) and is a characteristic peak unique to antigorite [27]. The above Raman features are the basis for the analysis of the phase transformation of antigorite in this study.

The characteristic Raman peaks for other reaction products such as talc, olivine, pyroxene, and Phase A are summarized in Supplementary Table S1.

2.4. Microscopic Observation

The microstructure reaction products are analyzed by scanning electron microscopy (SEM). The chemical compositions were analyzed by electron microprobe analysis (EMPA) on an X-ray electron probe microanalyzer (JXA-8230, JEOL Ltd., Tokyo, Japan) with acceler-

ating voltages of 15 kV, beamed current of 20 nA, microbeam diameters in the range of 1 to 3 μm , peak counting times of 20 s, and background counting times of 10 s. The lower limit of detection for all elements is 0.01%. The samples were fixed to aluminum stakes by colloid and then plated with a carbon film approximately 500 \AA . Then, the microstructure of reaction products was observed at Phenom-ProX scanning electron microscopy (SEM). The above sample preparation and analysis were performed at the Institute of Deep-Sea Science and Engineering, Chinese Academy of Sciences (CAS).

3. Results

Twenty-two experiments on the dehydration of antigorite were carried out; experimental conditions, P – T conditions for phase transitions, as well as post dehydration products are summarized in Table 2. The phase change products are confirmed based on Raman spectroscopy and electron probe analyses. The characteristic Raman peaks of the minerals from this study, including comparison with previous studies [28–32] and the composition of typical reaction minerals are summarized in Supplementary Tables S1 and S2, respectively.

Table 2. Experimental conditions and antigorite dehydration results.

Run No.	T _{range} (K)	P _{range} (GPa)	Phase Transition Point P(GPa)/T(K)	Recorded Spectra	Post Dehydration Products
DD0154	808–822	0.4–1.7	0.5/820	Yes	Atg, Tlc, Fo
DD0182	838–842	0.5–1.6	0.7/838	Yes	Atg, Tlc, Fo
DD0195	872	0.4	—	No	Tlc, Fo
DD0150	912	7.5	—	No	Fo, Cen
DD0178	760–985	3.4–7.5	7/896	Yes	Atg, Fo, Cen
DD0180	925	6.7	—	No	Fo, Cen
DD0187	705–1014	3.6–5.1	5/903	Yes	Atg, Fo, Cen
DD0188	924	4.4	—	No	Fo, Cen
DD0194	722–1062	1.6–3.4	3/958	Yes	Atg, Fo, Cen
DD0199	810–1065	2–3.5	2.7/976	Yes	Atg, Fo, Cen
DD0201	987	2.5	—	No	Fo, Cen
DD0205	701–1020	1.2–2.2	1.9/913	Yes	Atg, Fo, Cen
DD0210	930	1.8	—	No	Fo, Cen
DD0152	711	9.4	—	No	PhA, Cen
DD0185	701–839	8.1–9.6	9/735	Yes	Atg, PhA, Cen
DD0192	939	8.6	—	No	PhA, Cen
DD0196	781–825	5.4–9.6	8.7/821	Yes	Atg, PhA, Cen
DD0208	882	8.6	—	No	PhA, Cen
DD0207	833–898	0.2–0.8	0.7/892	Yes	Tlc, Fo, Cen
DD0155	875–941	5.5–9.8	7.9/930	Yes	Fo, PhA, Cen
DD0202	892–989	5.3–9.6	8.9/1035	Yes	Fo, PhA, Cen
DD0211	908–1060	5.4–10	8.6/980	Yes	Fo, PhA, Cen

PhA = phase A, Atg = antigorite, Fo = forsterite, and Cen = clinoenstatite.

In order to search for the P – T conditions of the starting point of dehydration reaction, in some initial runs, attention was mainly paid to monitoring experimental P – T conditions and the emergence of new phases from reading spectra. In these runs, Raman spectra only recorded the initial and final stages, not the whole process.

According to the phase change pressure, the dehydration process of antigorite can be divided into three pressure zones: low (0.4–0.7 GPa), medium (1.8–7.5 GPa), and high (8.6–9 GPa). Through the analysis of the dehydrated products, the three pressure ranges correspond to phase change Equations (1)–(3), respectively. These three dehydration processes will be elaborated in detail next.

3.1. Phase Transition at Low Pressures

For antigorite sample, at room pressure, four Raman spectral peaks at 228, 375, 682, and 1048 cm^{-1} appear in the low wavenumber region (Figures 5a, 8 and 11a), representing

O-H-O vibrations, bending vibrational mode of silicon-oxygen tetrahedral, symmetric stretching mode of the Si-O-Si group, and antisymmetric stretching mode of the Si-Ob-Si group, respectively [25–27,33]; two strong peaks at 3663 cm^{-1} and 3691 cm^{-1} can be seen in the high wavenumber region ($3550\text{--}3850\text{ cm}^{-1}$) (Figures 5a, 8 and 11a), representing the inner and outer hydroxyl groups, respectively [34].

During the experiments, Raman spectra were recorded from room temperature, and all the Raman spectral peaks of antigorite moved toward higher wavenumbers with the increase in pressure and temperature (Figure 5a). Meanwhile, the intensity of the Raman peaks of antigorite decreased significantly, and the Raman peak was broadened and blurred. With further heating and pressurization until the phase transition P - T conditions, some Raman peaks disappeared, together with the appearance of characteristic peaks of the dehydrated phase transformation products.

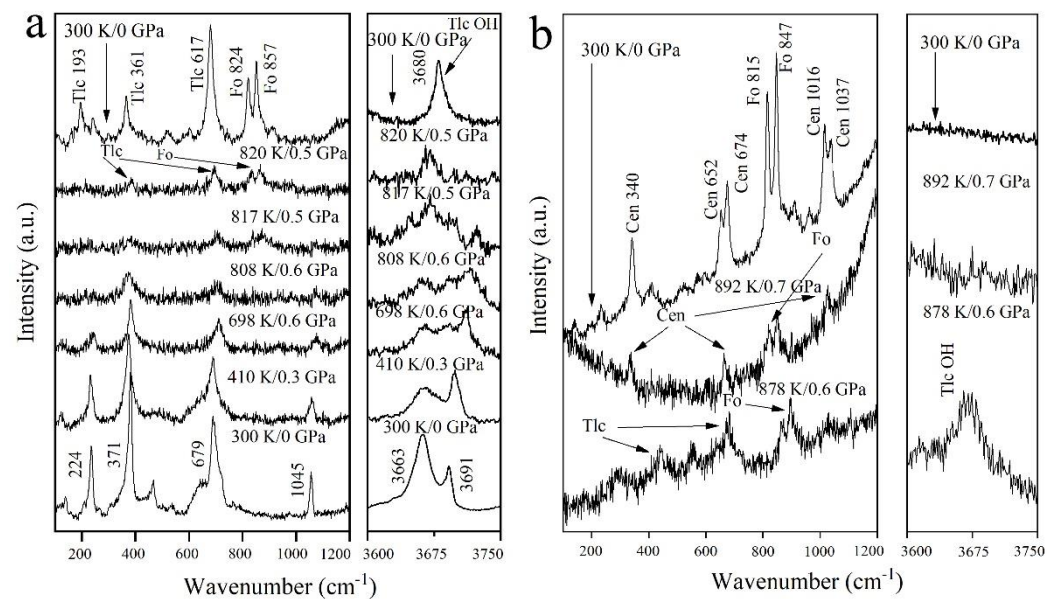


Figure 5. Representative Raman spectra collected from the dehydration phase transition process of antigorite, in both low and high wavenumber regions ($100\text{--}1200\text{ cm}^{-1}$, $3600\text{--}3675\text{ cm}^{-1}$), from the runs carried out at low pressures. P - T conditions for the collection of each spectrum are marked aside. (a) Run DD0154: reaction 1: $\text{Atg} = \text{Tlc} + \text{Fo} + \text{H}_2\text{O}$; (b) Run DD0207: $\text{Tlc} + \text{Fo}_{(\text{more})} = \text{Fo}_{(\text{less})} + \text{Cen} + \text{H}_2\text{O}$. In both cases, the appearance of new characteristic peaks of the reaction products (shown by arrows) indicates the occurrence of the reactions. Spectra for samples before and after each run are included for comparison. Atg = antigorite, Fo = forsterite, Tlc = talc, and Cen = clinoenstatite.

Our experiments show that, at low pressures ($P \leq 1\text{ GPa}$), antigorite stays stable only at temperatures below 800 K. With an increase in temperature, antigorite dehydrates first to talc + forsterite (Equation (1)) and then, at $\sim 900\text{ K}$, post dehydration products transit to forsterite + clinoenstatite (Equation (2)).

As shown in Figure 6, runs DD0154 and DD0182 represent the dehydration phase transition of antigorite to talc and forsterite; while run DD0207 represents the transformation of the talc-like and forsterite phases to forsterite and clinoenstatite. As shown by the arrows in Figure 5a, at 0.5 GPa and 820 K, the characteristic peaks from 100 to 1200 cm^{-1} about antigorite disappeared, and some new mixed Raman peaks of forsterite and talc appeared. The occurrence of olivine was confirmed after quenching by the SEM and EMPA (Figure 7a). Meanwhile, in the high wavenumber region, the hydroxyl characteristic peaks near 3663 cm^{-1} and 3691 cm^{-1} about antigorite disappeared, and a talc hydroxyl mode appeared. The Raman spectra of the talc phase disappeared and characteristic peaks of forsterite appeared as the temperature increased. At 892 K and 0.7 GPa, the main characteristic peaks of the

talc phase disappeared in the 100–1200 cm^{-1} region, and the characteristic peaks of olivine and clinoenstatite appeared (Figure 5b). At the same time, the hydroxyl peaks in the high wavenumber region 3600–3750 cm^{-1} disappeared (Figure 5b).

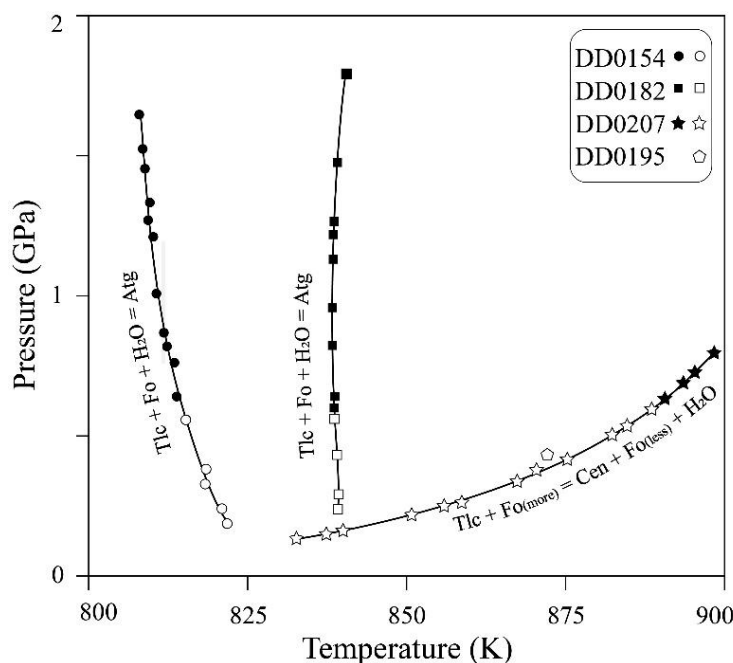


Figure 6. Dehydration phase transformation of antigorite under low pressures. Each line represents a run, and each point on the line represents the phase checkpoint based on in-situ Raman analyses. The equation describing the phase transition is marked by each line. Solid black circles, solid black squares, and solid black pentagon stand for antigorite (Atg); open symbols represent the appearance of talc (Tlc) and forsterite (Fo); and solid pentagrams represent the appearance of forsterite (Fo) and clinoenstatite (Cen).

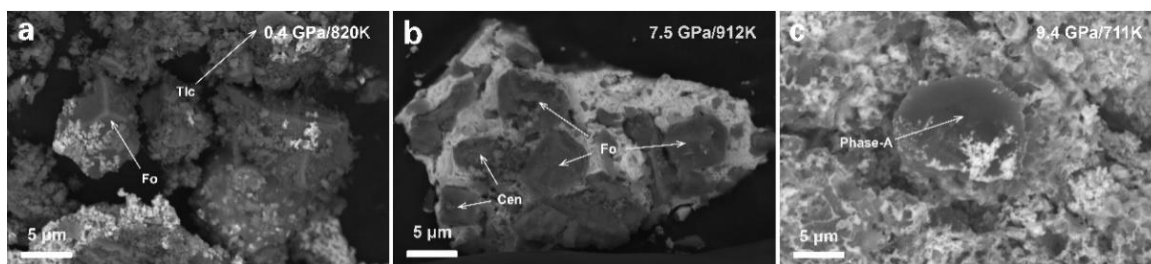


Figure 7. SEM images of products after in situ dehydration phase transition of antigorite at different temperature and pressure conditions. (a) forsterite (Fo) and talc (Tlc) at 0.4 GPa/820 K; (b) forsterite (Fo) and clinoenstatite (Cen) at 7.5 GPa/912 K; and (c) clinoenstatite (Cen) and phase A (PhA) at 9.4 GPa/711 K.

3.2. Phase Transition at Medium Pressures

At moderate pressures (1.8–7.5 GPa), as the temperature increases, antigorite dehydrates directly to forsterite + clinoenstatite (Equation (2)) at ~900 K. Exceptionally, in a narrow pressure range from 2–3 GPa, antigorite can stay stable up to ~960 K.

At 896 K and 7 GPa, the characteristic peaks of antigorite within 100 to 1200 cm^{-1} disappeared, and new Raman peaks appeared (Figure 8). Meanwhile, the hydroxyl peaks of antigorite at 3600 to 3750 cm^{-1} disappear in the high wavenumber region (Figure 8), indicating that a dehydration phase transition occurred accompanied by the dehydration of a large amount of water and the formation of new products. The new products forsterite and clinoenstatite crystal appears with a length of 7 μm and a width of 5 μm (Figure 7b).

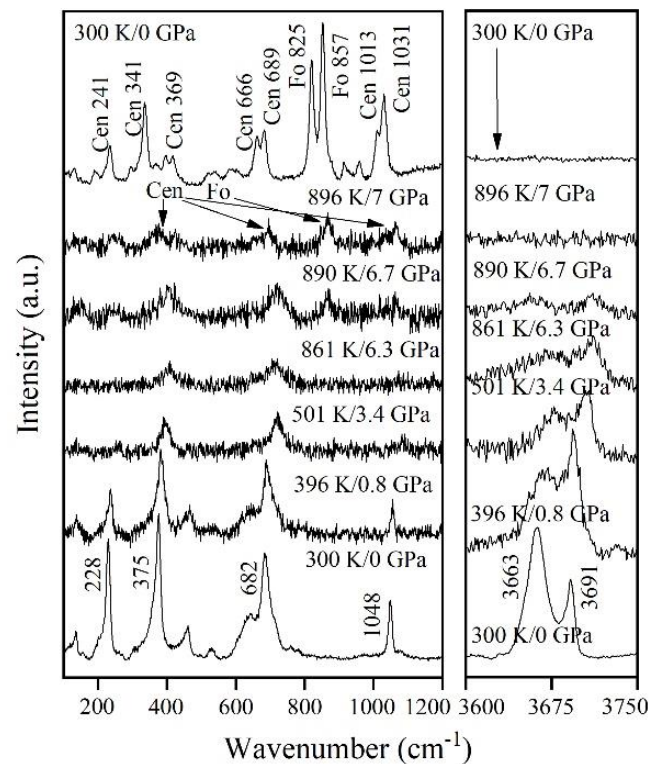


Figure 8. Representative Raman spectra collected from the dehydration phase transition process of antigorite, in both low and high wavenumber regions ($100\text{--}1200\text{ cm}^{-1}$, $3600\text{--}3750\text{ cm}^{-1}$), from the run DD0178 carried out at medium pressures. P – T conditions for the collection of each spectrum are marked aside. Run DD0178: reaction 2: $\text{Atg} = \text{Cen} + \text{Fo} + \text{H}_2\text{O}$. The appearance of new characteristic peaks of the reaction products (shown by arrows) indicates the occurrence of the reactions. Spectra for samples before and after each run are included for comparison. Atg = antigorite, Fo = forsterite, and Cen = clinoenstatite.

In Figure 9, runs DD0178, DD0187, DD0194, DD0199, and DD0205 represent the experimental curves for the phase transformation from antigorite into forsterite and clinoenstatite.

3.3. Phase Transition at High Pressures

At high pressures ($P > 8.5\text{ GPa}$), as the increase in temperature, antigorite dehydrates directly to clinoenstatite + phase A (reaction 3).

Runs DD0185 and DD0196 recorded the dehydration phase transition process of Equation (3): $\text{Atg} = \text{PhA} + \text{Cen} + \text{H}_2\text{O}$ (Figure 10). While runs DD0211, DD0202, and DD0155 reflected the transformation from forsterite and clinoenstatite to phase A and clinoenstatite. For run DD0196, at 821 K and 8.7 GPa, the main characteristic peak of antigorite at 100 to 1200 cm^{-1} disappeared, and the Raman peak of phase A and clinoenstatite appeared (Figure 11a). Meanwhile, the characteristic peak of antigorite hydroxyl at the high wavenumber region $3250\text{ to }3800\text{ cm}^{-1}$ disappeared, and phase A hydroxyl mode appeared (Figure 11a). Phase A was confirmed by EMPA and SEM (Figure 7c and Table S2). In addition, the transition reaction from forsterite and clinoenstatite to clinoenstatite and phase A could occur by rapid pressurization (Figure 11b). At 971 K and 8.2 GPa, the main characteristic peak of forsterite disappears at $100\text{ to }1200\text{ cm}^{-1}$, and clinoenstatite and phase A Raman peak appeared (Figure 11b). Moreover, phase A hydroxyl mode appeared in the high wave number region at $3250\text{ to }3550\text{ cm}^{-1}$ (Figure 11b).

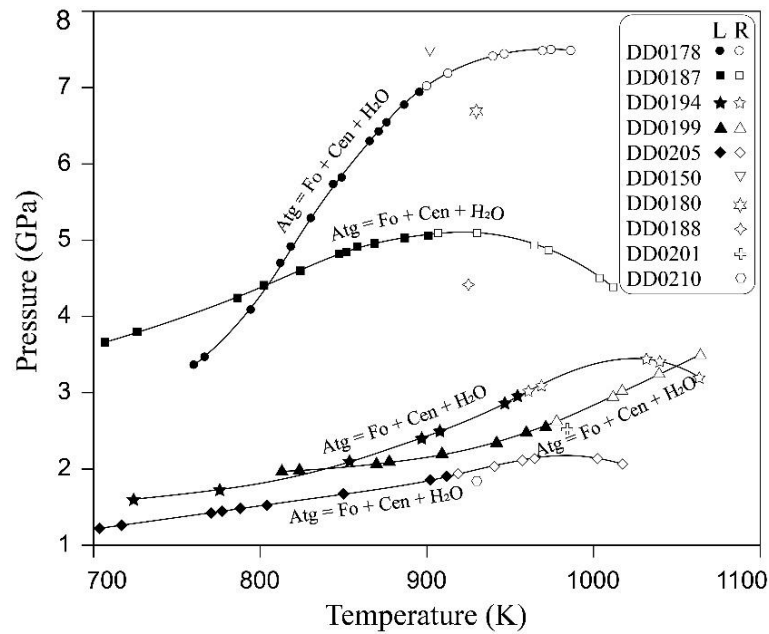


Figure 9. Dehydration phase transformation of antigorite under medium pressures. Each line represents a run, and each point on the line represents the phase checkpoint based on in-site Raman analyses. The equation describing the phase transition is marked by each line. Those points in the solid symbol represent the reactant on the left (L) of the equation, and the open symbol represents the appearance of the product on the right (R) of the equation.

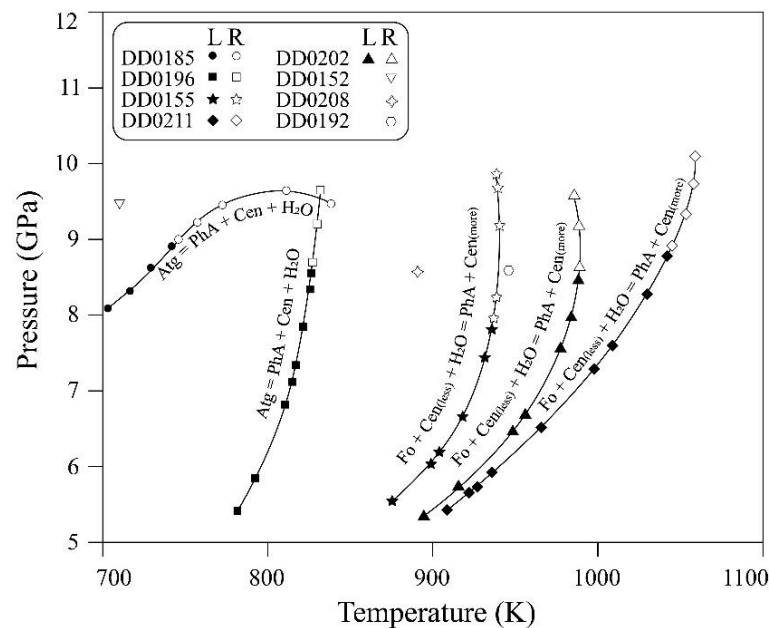


Figure 10. Dehydration phase transformation of antigorite under high pressures. Each line represents a run, and each point on the line represents the phase checkpoint based on in-site Raman analyses. The equation describing the phase transition is marked by each line. Those points in the solid symbol represent the reactant on the left (L) of the equation, and the open symbol represents the appearance of the product on the right (R) of the equation.

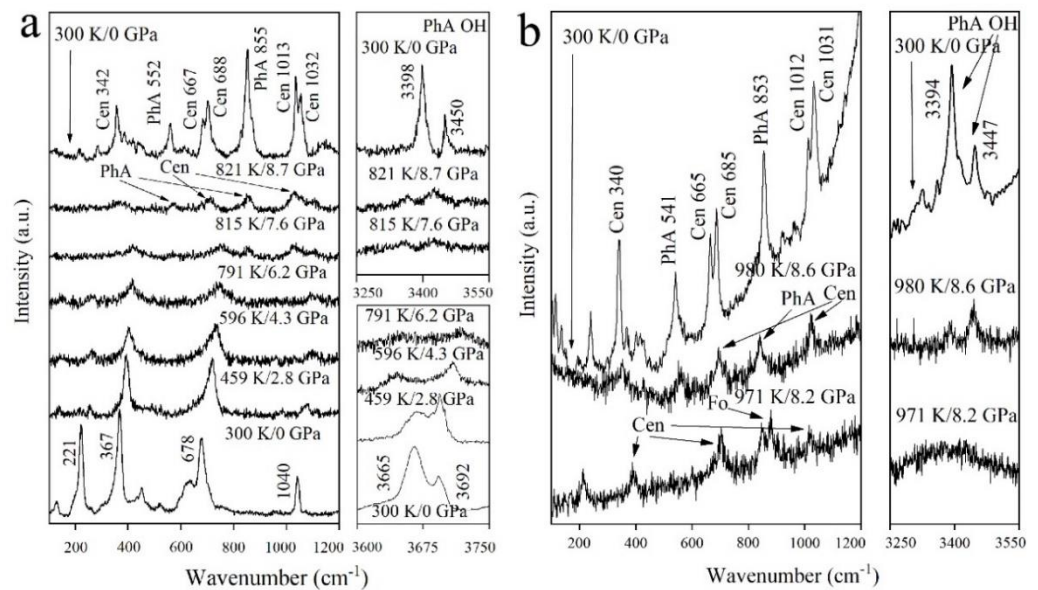


Figure 11. Representative Raman spectra collected from the dehydration phase transition process of antigorite, in both low and high wavenumber regions ($100\text{--}1200\text{ cm}^{-1}$, $3600\text{--}3675\text{ cm}^{-1}$), from the runs carried out at high pressures. *P*–*T* conditions for the collection of each spectrum are marked aside. (a) Run DD0196: reaction 3: $\text{Atg} = \text{PhA} + \text{Cen} + \text{H}_2\text{O}$; (b) Run DD0211: $\text{Cen}_{(\text{less})} + \text{Fo} \rightarrow \text{PhA} + \text{Cen}_{(\text{more})}$. In both cases, the appearance of new characteristic peaks of the reaction products (shown by arrows) indicates the occurrence of the reactions. Spectra for samples before and after each run are included for comparison. Atg = antigorite, Fo = forsterite, PhA = phase A, and Cen = clinoenstatite.

3.4. Microscopic Analyses of Dehydration Phase Transformation Products

The dehydration products of antigorite were analyzed by SEM. Wormlike fissures and pores formed during dehydration (Figure 12a–c). In run DD0180, pores formed at 6.7 GPa/925 K. Most of the pores are approximately 5 μm in diameter, and individual tiny pores are about 1 μm in diameter (Figure 12a). Wormlike fissure formed after dehydration at 2.5 GPa at 987 K in run DD0201 (Figure 12b) and at 4.4 GPa/924 K in run DD0188 (Figure 12c). It is speculated that these fissures are channels formed by the flow of water.



Figure 12. SEM images of dehydration products of antigorite. (a) Small pores caused by the fluid during dehydration phase transition at 6.7 GPa/925 K; (b) wormlike fissures formed after dehydration phase transition at 2.5 GPa/987 K; and (c) large fluid channel formed at 4.4 GPa/924 K. Fo = forsterite, Cen = clinoenstatite, PhA = phase A, and Tlc = talc.

4. Discussion

4.1. The Difference between This Study and Predecessors on the Stable Domain of Antigorite

Based on the experimental results, the phase diagram for the dehydration of antigorite, at pressures up to 10 GPa and temperatures up to 1100 K, is summarized in Figure 13. Compared with previous studies, the dehydration process of antigorite characterized in this study is somewhat different.

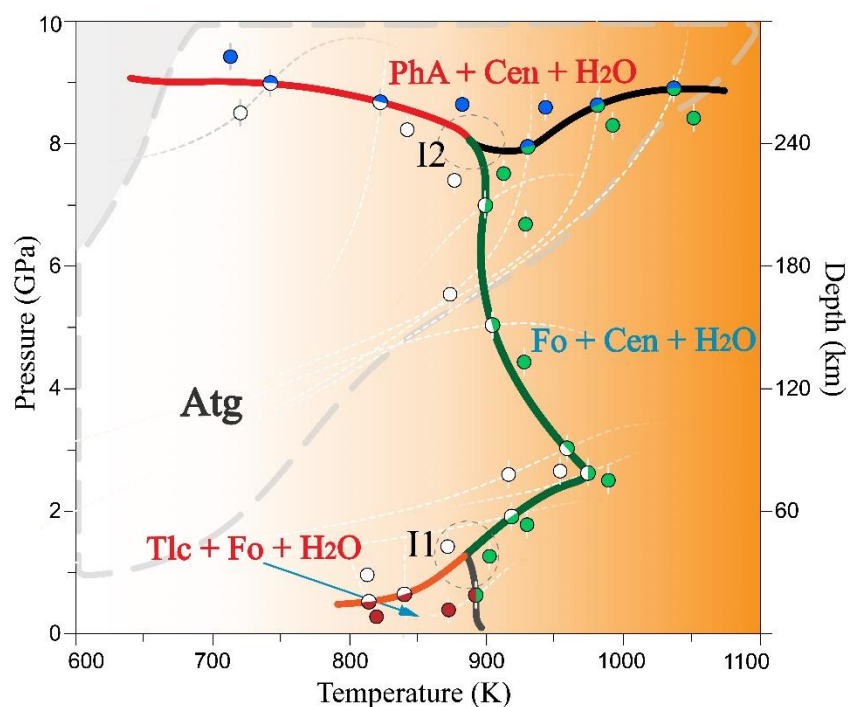


Figure 13. Phase transformation diagram of antigorite. Solid white, red, green, and blue circles represent the stable domain of antigorite (Atg), the coexistence of talc (Tlc) and forsterite (Fo), the coexistence of forsterite (Fo) and clinoenstatite (Cen), and the coexistence of phase A (PhA) and clinoenstatite (Cen), respectively. The solid circles with half white and half red indicate the occurrence of reaction 1: $\text{Atg} = \text{Tlc} + \text{Fo} + \text{H}_2\text{O}$; the solid circles with half white and half green represent that reaction 2: $\text{Atg} = \text{Fo} + \text{Cen} + \text{H}_2\text{O}$ occurs; the solid circles with half white and half blue mean that the dehydration phase transition reaction 3: $\text{Atg} = \text{PhA} + \text{Cen} + \text{H}_2\text{O}$ occurs; the solid circles with half red and half green represent the boundary where the transformation from Tlc + Fo to Fo + Cen occurs; and the solid circles with half blue and half green indicate the boundary where the transformation Fo + Cen + H₂O to Cen + PhA happens. The height of the white vertical line at the solid circle gives the uncertainty of the pressure measurements in the experiment, and the white dashed line indicates the trajectory of temperature and pressure changes inside the pressure chamber during in situ observations. The *P-T* conditions in the grey area are considered to not exist during subduction. The area bounded by the grey dashed line represents geothermal conditions in cold subduction zones where antigorite may be stable, but the antigorite can transfer to phase A and clinoenstatite at high *P-T* conditions at this area.

First, in our study, it found that reaction 2, $\text{Atg} = \text{Fo} + \text{Cen} + \text{H}_2\text{O}$, has a positive *P/T* slope when the pressure is lower than 2.5 GPa and a negative *P/T* slope when the pressure is greater than approximately 2.5 GPa (Figure 13). The reason for this is unclear and needs to be further investigated through specially designed experiments.

Second, the five reactions mentioned above which are related to the dehydration process of antigorite were identified in this study and the triple points, I1 and I2, associated with those reactions were determined. At this point, our study is, in general, consistent with previous ones. However, the *P-T* conditions for these two triple points determined by this study are quite different from others. The I1 and I2 in this study are at 1.3 GPa/870 K and 8.2 GPa/870 K, respectively, which are very different from the previous results (shown in Figure 1). The I2 determined by the experiment conducted on the multi anvil press or piston-cylinder press from Bose and Navrotsky (1998) [20], Ulmer and Trommsdorff (1995) [17], and Wunder and Schreyer (1997) [18] are at 5.8 GPa/893 K, 6.6 GPa/843 K, and 4.2 GPa/858 K, respectively [17,18,20]. In particular, the pressure for I2 in all previous studies is much lower than that in this study.

There are four possible reasons for the above differences. The first reason may be due to the difference in the composition of antigorite. As the iron content increases, the thermal stability of antigorite decreases [35]. At 1.8 GPa, the stable boundary for antigorite with a high aluminum content (e.g., 3.7 wt.%) is 60–70 K higher than non-aluminum antigorite [18]. The phase transformation from antigorite with an FeO content of 4.15% to forsterite and talc occurs at 843 K and 1.1 GPa [19]. On the contrary, this happens at 878 K and 1.1 GPa for antigorite with an FeO content of 1.99% in this paper. It is reasonable that the high FeO content may be a factor in reducing the stability domain of antigorite. The FeO* content of the antigorite used in this study is nearly the same as that of Wunder and Schreyer (1997) [18], but its Al₂O₃ content is 0.68%, which is much lower than the value of 2.96% in this paper. The I2 point of Wunder and Schreyer (1997) [18] is at 5.2 GPa/763 K, which is much lower than the value of 8.2 GPa/873 K in this paper. The difference for the I2 location seems to be a result of the high Al content. However, the I1 point of Wunder and Schreyer (1997) [18] is at 1.5 GPa/913 K, with a higher stability domain than this paper (1.3 GPa/873 K), which contradicts the perception that higher Al content leads to an increased stability domain. We speculate that, although the Fe and Al content may contribute to the difference in the stability domain, it should not be the main reason.

The second reason could be the difference in the heating and pressurizing devices. The pressure calibration material ¹³C diamond used in this experiment had a pressure measurement error of about ± 0.3 GPa [22], and the DAC, with outside heating, had a precise temperature control (error of approximately ±1 K) and a small thermal gradient due to the good thermal conductivity of the diamond [36]. On the contrary, the temperature errors in large volume presses are large, e.g., the temperature gradient inside the graphite heating furnace was 20–100 K/mm, and inside the LaCrO₃ heating furnace was 50–200 K/mm for a multi anvil press, with an octahedral side length of 18 mm at 1773 K [37].

The third reason may be due to the difference of water activity. Previous studies reveal that the high-temperature stability limit of antigorite is decreased by 50–100 K under H₂O-unsaturated conditions [38]. On the premise of maintaining low water activity, the dehydration reaction will be enhanced, so that the whole dehydration process can be completed in a shorter time, but this is almost impossible under the condition of water saturation. Compared with the experiment in large volume press and water as the pressure medium, the use of argon pressure medium may result in low water fugacity in the reaction environment, which logically leads to a reduction in the stable region of serpentine. However, the stability domain of the antigorite in this research is significantly higher than that of the large volume press, so we believe that the difference between the experimental results of this paper and the large volume press may not be caused by water activity.

The fourth reason may be the difference of characterization means. According to previous large volume press studies on dehydration kinetics of antigorite [19,39], dehydration takes a long time at conditions near the dehydration phase boundary; for example, dehydration occurred within 2 h at 913 K below 6 GPa when the *P–T* path moved into the region of forsterite + pyroxene + H₂O [39]. Previous phase equilibrium studies [18,40] generally had a much longer duration of 10–100 h. In this study, the pressurization time varies from 1000 to 2000 s, which is much shorter than that of large volume press. Longer reaction times may reduce the temperature and pressure values of the phase transition. In this study, the whole dehydration process of antigorite was observed in situ by on-line Raman spectroscopy analysis under real-time high temperature and pressure conditions using a dynamic loading device for the first time. Phase transitions can occur instantaneously. The pressure within the system was slowly varied in real-time until the phase transition pressure threshold was reached. In contrast, pre-quench temperature and pressure values conducted on a multi anvil press or piston-cylinder press are thought to be the phase transition *P–T* conditions. In this method, if the dehydration phase transition occurs in the system before the recorded *P–T* values, and the *P–T* conditions for the dehydration phase transition are lower than the recorded *P–T* values, this could lead to considerable errors in these experiments. In addition, during the quenching process, some inverse reaction could

happen which could lead to an incomplete reaction during analysis. This can also lead to misjudgments about the position of dehydration phase transition. The use of dynamic in situ observation techniques fundamentally avoided this phenomenon and minimized all errors associated with the quenching process.

4.2. Relationship between Dehydration Phase Transition of Antigorite and Earthquakes

Earthquakes can be divided into three categories according to depth: shallow-focus earthquakes with a depth of <70 km, intermediate-focus earthquakes with a depth of 70–300 km, and deep-focus earthquakes with a depth of >300 km [38,41]. Dehydration embrittlement [42,43] and plastic shear instability [44–46] are thought to be the prevailing cause of intermediate-focus earthquakes. The concept of dehydration embrittlement was introduced by Raleigh and Paterson (1965) [43,47,48]. Embrittlement is caused by the reduction in effective envelope pressure due to the pore pressure of the water released and the loss of cohesive strength due to structural changes during dehydration [43]. Sawai et al. (2013) suggested that the dehydration of antigorite can be approximated as a matter of one-dimensional diffusion and found that the rate of antigorite dehydration was more than 100 times faster than the rate of relaxation, which is sufficient to induce intermediate-focus earthquakes at the lower levels of the double seismic zone [4]. However, some scholars hold the view that the dehydration of antigorite may not be a direct cause of intermediate-focus earthquakes within the subduction zone [49–51]. It is likely that the water generated by dehydration is forced into the brittle surrounding rocks, causing a dramatic increase in pore pressure in the surrounding rocks and a decrease in the effective positive stress on the rupture surface, which triggers the earthquake [52,53].

In this study, wormlike fissures and pores produced by dehydration are found in all samples after experimental quenching (Figure 12). Combining experimental phenomena and previous views, this paper suggests that there are two possible mechanisms for causing intermediate-focus earthquakes: (1) The water in the wormlike fissures and pores produced by the dehydration of antigorite causes a macroscopic slip; (2) water may also flow into the brittle surrounding rock, causing a “collapse” of the empty fissures and pores, which in turn can cause earthquakes. It is clear that the dehydration of antigorite can indeed cause brittle fractures and is an important cause of intermediate-focus earthquakes.

5. Conclusions

(1) The precise phase boundaries for the dehydration of antigorite are determined by the dynamic diamond anvil cell and in situ Raman spectrum study. The dehydration process is pressure dependent. At low pressures (<0.7 GPa), antigorite transfers to talc and forsterite; as the temperature increases, the talc disappears and a combination of forsterite and clinoenstatite occurs. At moderate pressures (1.8–7.5 GPa), antigorite dehydrates directly into forsterite and clinoenstatite with increasing temperature. At high pressures (>8.6 GPa), the products of the dehydration phase transition of antigorite are clinoenstatite and phase A.

(2) The triple points of I1 and I2 for the dehydration phase transition of antigorite determined in this study are at 1.3 GPa/870 K and 8.2 GPa/870 K, respectively.

(3) The reaction (Antigorite → Forsterite + Clinoenstatite + H₂O) phase transition curve has a negative P/T slope if the pressure is greater than approximately 2.5 GPa and a positive P/T slope when the pressure is lower than 2.5 GPa.

(4) Wormlike fissures and pores were found in all dehydrated antigorite samples, which supports the hypothesis that dehydration embrittlement may lead to intermediate-depth earthquakes.

Supplementary Materials: The following supporting information can be downloaded at: <https://www.mdpi.com/article/10.3390/min12050567/s1>, Table S1: Summary of characteristic Raman peaks of typical minerals in the antigorite dehydration; Table S2: Composition (wt.%) of reaction products in antigorite dehydration

Author Contributions: Conceptualization, S.L.; methodology, S.L.; software, S.L.; validation, S.L.; formal analysis, S.L.; investigation, S.L. and Y.L.; resources, S.M.; data curation, S.M.; writing—original draft preparation, S.L.; writing—review and editing, S.L., Y.L. and S.M.; visualization, S.L.; supervision, S.M.; project administration, S.M.; funding acquisition, S.M.. All authors have read and agreed to the published version of the manuscript.

Funding: This study was financially supported by the Chinese Academy of Sciences (Grants No. QYZDY-SSW-DQC029 and No. XDA22040501).

Acknowledgments: We are very grateful to anonymous reviewers for their great help in improving this manuscript and constructive opinions. Liping Wang is acknowledged for their great assistance in the synthesis of ^{13}C diamond. This study was financially supported by the Chinese Academy of Sciences (Grants No. QYZDY-SSW-DQC029 and No. XDA22040501).

Conflicts of Interest: We declare that we have no conflict of interest.

References

1. Guillot, S.; Hattori, K.H.; de Sigoyer, J. Mantle wedge serpentinization and exhumation of eclogites: Insights from eastern Ladakh, northwest Himalaya. *Geology* **2000**, *28*, 199–202. [[CrossRef](#)]
2. Evans, B.W.; Hattori, K.; Baronnet, A. Serpentinite: What, why, where? *Elements* **2013**, *9*, 99–106. [[CrossRef](#)]
3. Hattori, K.; Guillot, S. Volcanic fronts form as a consequence of serpentinite dehydration in the forearc mantle wedge. *Geology* **2003**, *31*, 525–528. [[CrossRef](#)]
4. Sawai, M.; Katayama, I.; Hamada, A.; Maeda, M.; Nakashima, S. Dehydration kinetics of antigorite using in situ high-temperature infrared microspectroscopy. *Phys. Chem. Miner.* **2013**, *40*, 319–330. [[CrossRef](#)]
5. Shen, T.; Zhang, L.; Chen, J. Metamorphism of subduction zone serpentinite. *Acta Petrol. Sin.* **2016**, *32*, 1206–1218.
6. Wu, K.; Yuan, H.; Lyu, N.; Zhang, L. The behavior of fluid mobile elements during serpentinization and dehydration of serpentinites in subduction zones. *Acta Petrol. Sin.* **2020**, *36*, 141–153.
7. Wicks, F.J.; O’Hanley, D.S. Chapter 5. Serpentine minerals: Structures and petrology. In *Hydrous Phyllosilicates*; De Gruyter: Berlin, Germany, 1988; Volume 19, pp. 91–168. [[CrossRef](#)]
8. Bose, K.; Ganguly, J. Experimental and theoretical studies of the stabilities of talc, antigorite and phase A at high pressures with applications to subduction processes. *Earth Planet. Sci. Lett.* **1995**, *136*, 109–121. [[CrossRef](#)]
9. Dódony, I.; Buseck, P.R. Serpentine Close-Up and Intimate: An HRTEM View. *Int. Geol. Rev.* **2004**, *46*, 507–527. [[CrossRef](#)]
10. Bailey, S.W. Hydrous Phyllosilicates—Introduction. *Rev. Mineral.* **1988**, *19*, 1–8.
11. Hilairet, N.; Reynard, B.; Wang, Y.; Daniel, I.; Merkel, S.; Nishiyama, N.; Petitgirard, S. High-Pressure Creep of Serpentine, Interseismic Deformation, and Initiation of Subduction. *Science* **2007**, *318*, 1910–1913. [[CrossRef](#)]
12. Hyndman, R.D.; Peacock, S.M. Serpentinization of the forearc mantle. *Earth Planet. Sci. Lett.* **2003**, *212*, 417–432. [[CrossRef](#)]
13. Kawano, S.; Katayama, I.; Okazaki, K. Permeability anisotropy of serpentinite and fluid pathways in a subduction zone. *Geology* **2011**, *39*, 939–942. [[CrossRef](#)]
14. Reynard, B.; Mibe, K.; Van de Moortèle, B. Electrical conductivity of the serpentinised mantle and fluid flow in subduction zones. *Earth Planet. Sci. Lett.* **2011**, *307*, 387–394. [[CrossRef](#)]
15. Rupke, L.H.; Morgan, J.P.; Hort, M.; Connolly, J.A.D. Serpentine and the subduction zone water cycle. *Earth Planet. Sci. Lett.* **2004**, *223*, 17–34. [[CrossRef](#)]
16. Scambelluri, M.; Bottazzi, P.; Trommsdorff, V.; Vannucci, R.; Hermann, J.; Gomez-Pugnaire, M.T.; Sanchez-Vizcaino, V.L. Incompatible element-rich fluids released by antigorite breakdown in deeply subducted mantle. *Earth Planet. Sci. Lett.* **2001**, *192*, 457–470. [[CrossRef](#)]
17. Ulmer, P.; Trommsdorff, V. Serpentine stability to mantle depths and subduction-related magmatism. *Science* **1995**, *268*, 858–861. [[CrossRef](#)]
18. Wunder, B.; Schreyer, W. Antigorite: High-pressure stability in the system MgO-SiO₂-H₂O (MSH). *Lithos* **1997**, *41*, 213–227. [[CrossRef](#)]
19. Perrillat, J.-P.; Daniel, I.; Koga, K.T.; Reynard, B.; Cardon, H.; Crichton, W.A. Kinetics of antigorite dehydration: A real-time X-ray diffraction study. *Earth Planet. Sci. Lett.* **2005**, *236*, 899–913. [[CrossRef](#)]
20. Bose, K.; Navrotsky, A. Thermochemistry and phase equilibria of hydrous phases in the system MgO-SiO₂-H₂O: Implications for volatile transport to the mantle. *J. Geophys. Res. Earth Surf.* **1998**, *103*, 9713–9719. [[CrossRef](#)]
21. Padrón-Navarta, J.A.; Hermann, J.; Garrido, C.J.; Sánchez-Vizcaino, V.L.; Gómez-Pugnaire, M.T. An experimental investigation of antigorite dehydration in natural silica-enriched serpentinite. *Contrib. Miner. Pet.* **2009**, *159*, 25–42. [[CrossRef](#)]
22. Munsch, P.; Bureau, H.; El Yakoubi, M.; Khodja, H.; Zaitsev, A. The use of ^{13}C diamond as pressure and temperature sensor for diamond-anvil-cell experiments. *Eur. J. Miner.* **2015**, *27*, 365–375. [[CrossRef](#)]
23. Chertkova, N.; Yamashita, S.; Ito, E.; Shimojuku, A. High-pressure synthesis and application of a ^{13}C diamond pressure sensor for experiments in a hydrothermal diamond anvil cell. *Miner. Mag.* **2014**, *78*, 1677–1685. [[CrossRef](#)]

24. Griffith, W.; Lesniak, P. Raman studies on species in aqueous solutions. Part III. Vanadates, molybdates, and tungstates. *J. Chem. Soc. A Inorg. Phys. Theor.* **1969**, *3*, 1066–1071. [[CrossRef](#)]
25. Kloprogge, J.T.; Frost, R.L.; Rintoul, L. Single crystal Raman microscopic study of the asbestos mineral chrysotile. *Phys. Chem. Chem. Phys.* **1999**, *1*, 2559–2564. [[CrossRef](#)]
26. Bahram, B.; Hesam, M.; Divya, P.; Iris, W. Raman characteristics of Alpine–Himalayan serpentine polymorphs: A case study of Khankuie ultramafic complex, southeast of Iran. *J. Earth Syst. Sci.* **2019**, *128*, 1–15. [[CrossRef](#)]
27. Kloprogge, J.T.; Wharton, D.; Hickey, L.; Frost, R.L. Infrared and Raman study of interlayer anions CO_3^{2-} , NO_3^- , SO_4^{2-} and ClO_4^- in Mg/Al-hydrotalcite. *Am. Mineral.* **2002**, *87*, 623–629. [[CrossRef](#)]
28. Chollet, M.; Daniel, I.; Koga, K.T.; Petitgirard, S.; Morard, G. Dehydration kinetics of talc and 10 Å phase: Consequences for subduction zone seismicity. *Earth Planet. Sci. Lett.* **2009**, *284*, 57–64. [[CrossRef](#)]
29. Debret, B.; Nicollet, C.; Andreani, M.; Schwartz, S.; Godard, M. Three steps of serpentinization in an eclogitized oceanic serpentinization front (Lanzo Massif–Western Alps). *J. Metamorph. Geol.* **2013**, *31*, 165–186. [[CrossRef](#)]
30. Likhacheva, A.Y.; Goryainov, S.V.; Rashchenko, S.V.; Dementiev, S.N.; Safonov, O.G. In situ observation of chrysotile decomposition in the presence of NaCl-bearing aqueous fluid up to 5 GPa and 400 °C. *Mineral. Petrol.* **2021**, *115*, 213–222. [[CrossRef](#)]
31. Lin, C.-C. Pressure-induced polymorphism in enstatite (MgSiO_3) at room temperature: Clinoenstatite and orthoenstatite. *J. Phys. Chem. Solids* **2004**, *65*, 913–921. [[CrossRef](#)]
32. Maurice, J.; Bolfan-Casanova, N.; Padrón-Navarta, J.; Manthilake, G.; Hammouda, T.; Hénot, J.; Andraut, D. The stability of hydrous phases beyond antigorite breakdown for a magnetite-bearing natural serpentinite between 6.5 and 11 GPa. *Contrib. Mineral. Petrol.* **2018**, *173*, 1–22. [[CrossRef](#)]
33. Griffith, W.; Wickins, T. Raman studies on species in aqueous solutions. Part I. The vanadates. *J. Chem. Soc. A Inorg. Phys. Theor.* **1966**, *1*, 1087–1090. [[CrossRef](#)]
34. Auzende, A.L.; Daniel, I.; Reynard, B.; Lemaire, C.; Guyot, F. High-pressure behaviour of serpentine minerals: A Raman spectroscopic study. *Phys. Chem. Miner.* **2004**, *31*, 269–277. [[CrossRef](#)]
35. Merkulova, M.; Munoz, M.; Vidal, O.; Brunet, F. Role of iron content on serpentinite dehydration depth in subduction zones: Experiments and thermodynamic modeling. *Lithos* **2016**, *264*, 441–452. [[CrossRef](#)]
36. Foustoukos, D.I.; Mysen, B.O. The structure of water-saturated carbonate melts. *Am. Miner.* **2015**, *100*, 35–46. [[CrossRef](#)]
37. Walter, M.J.; Thibault, Y.; Wei, K.; Luth, R.W. Characterizing experimental pressure and temperature conditions in multi-anvil apparatus. *Can. J. Phys.* **1995**, *73*, 273–286. [[CrossRef](#)]
38. Green, H.W.; Houston, H. The mechanics of deep earthquakes. *Annu. Rev. Earth Planet. Sci.* **1995**, *23*, 169–213. [[CrossRef](#)]
39. Inoue, T.; Yoshimi, I.; Yamada, A.; Kikegawa, T. Time-resolved X-ray diffraction analysis of the experimental dehydration of serpentine at high pressure. *J. Miner. Pet. Sci.* **2009**, *104*, 105–109. [[CrossRef](#)]
40. Komabayashi, T.; Hirose, K.; Funakoshi, K.-I.; Takafuji, N. Stability of phase A in antigorite (serpentine) composition determined by in situ X-ray pressure observations. *Phys. Earth Planet. Inter.* **2005**, *151*, 276–289. [[CrossRef](#)]
41. Frohlich, C. The nature of deep-focus earthquakes. *Annu. Rev. Earth Planet. Sci.* **1989**, *17*, 227–254. [[CrossRef](#)]
42. Jung, H.; Green, H.W. Experimental Faulting of Serpentinite during Dehydration: Implications for Earthquakes, Seismic Low-Velocity Zones, and Anomalous Hypocenter Distributions in Subduction Zones. *Int. Geol. Rev.* **2004**, *46*, 1089–1102. [[CrossRef](#)]
43. Raleigh, C.B.; Paterson, M.S. Experimental deformation of serpentinite and its tectonic implications. *J. Geophys. Res. Earth Surf.* **1965**, *70*, 3965–3985. [[CrossRef](#)]
44. Kelemen, P.B.; Hirth, G. A periodic shear-heating mechanism for intermediate-depth earthquakes in the mantle. *Nature* **2007**, *446*, 787–790. [[CrossRef](#)] [[PubMed](#)]
45. Deseta, N.; Andersen, T.; Ashwal, L. A weakening mechanism for intermediate-depth seismicity? Detailed petrographic and microtextural observations from blueschist facies pseudotachylytes, Cape Corse, Corsica. *Tectonophysics* **2014**, *610*, 138–149. [[CrossRef](#)]
46. John, T.; Medvedev, S.; Rüpke, L.H.; Andersen, T.B.; Podladchikov, Y.; Austrheim, H. Generation of intermediate-depth earthquakes by self-localizing thermal runaway. *Nat. Geosci.* **2009**, *2*, 137–140. [[CrossRef](#)]
47. Fukumura, S.; Okamoto, K.; Terabayashi, M. Metamorphic olivine after dehydration embrittlement in Serpentinite: Case study from the Shiraga Serpentinite mass in the Sanbagawa high P/T metamorphic belt, central Shikoku, Japan. *Island Arc* **2019**, *28*, e12293. [[CrossRef](#)]
48. Yamasaki, T.; Seno, T. Double seismic zone and dehydration embrittlement of the subducting slab. *J. Geophys. Res. Solid Earth* **2003**, *108*, 1–21. [[CrossRef](#)]
49. Chernak, L.J.; Hirth, G. Deformation of antigorite serpentinite at high temperature and pressure. *Earth Planet. Sci. Lett.* **2010**, *296*, 23–33. [[CrossRef](#)]
50. Chernak, L.J.; Hirth, G. Syndeformational antigorite dehydration produces stable fault slip. *Geology* **2011**, *39*, 847–850. [[CrossRef](#)]
51. Shao, T.; Zhou, Y.; Song, M.; Ma, X.; Zhang, L.; Yao, W.; Dang, J.; Li, J. Deformation of Antigorite and Its Geological Implications. *J. Geophys. Res. Solid Earth* **2021**, *126*, e2021JB021650. [[CrossRef](#)]
52. Arkwright, J.; Rutter, E.; Brodie, K.; Llana-Fúnez, S. Role of porosity and dehydration reaction on the deformation of hot-pressed serpentinite aggregates. *J. Geol. Soc.* **2008**, *165*, 639–649. [[CrossRef](#)]
53. Rutter, E.; Llana-Fúnez, S.; Brodie, K. Dehydration and deformation of intact cylinders of serpentinite. *J. Struct. Geol.* **2009**, *31*, 29–43. [[CrossRef](#)]